Three-Dimensional Phase-Field Simulation and Experimental Validation of β-Mg$_{17}$Al$_{12}$ Phase Precipitation in Mg-Al-Based Alloys

GUOMIN HAN, ZHIQIANG HAN, ALAN A. LUO, and BAICHENG LIU

A three-dimensional (3D) phase-field model has been developed to simulate the formation of lath-shaped β-Mg$_{17}$Al$_{12}$ phase during hcp$\rightarrow$bcc transformation in Mg-Al-based alloys. The model considers the synergistic effects of the elastic strain energy associated with the lattice rearrangements that accompany the phase transformation, and the interface anisotropy (both in interfacial energy and interface mobility coefficient). By using the proposed model, the essential features of 3D morphology of the β phase precipitate have been successfully predicted and experimentally validated using high-resolution transmission electron microscopy and atomic force microscopy. Furthermore, the spatial distribution of anisotropic elastic interaction field around a pre-existing β precipitate has been quantitatively determined using 3D phase-field simulation, and the effects of the anisotropic elastic interaction energy on subsequent nucleation of β phase near a pre-existing precipitate have been revealed. The results suggest that the anisotropic elastic interaction energy can promote the formation of new nucleus near the lozenge ends of the pre-existing precipitate, as explicitly substantiated by the experimental observations. The influence of different combinations of interface anisotropy and elastic strain energy on the thickness of β phase precipitate has been elucidated. The correlation between microstructural design during precipitation and the alloy-strengthening mechanisms has also been discussed in terms of dislocation motion. Based on these results, possible strategies for strengthening Mg-Al-based alloys are proposed for magnesium alloy development and microstructural design.

I. INTRODUCTION

MAGNESIUM alloys are characterized by their low density, high specific strength, and excellent castability, making them ideal structural materials for lightweight applications, especially in the transportation industries.[1,2] The most popular commercial cast alloy, known as AZ91, is based on the composition Mg-9Al-1Zn (all compositions in wt pct except when stated otherwise). Compared with binary Mg-Al alloys, the ternary AZ91 alloy has no major new phases[3] in the as-cast microstructure, because the Al to Zn ratio in this alloy is greater than 3:1.[4] According to the Mg-Al binary phase diagram, eutectic β phase dissolves during solution treatment and forms precipitates during the subsequent aging process.[3–5] The β phase is a stoichiometric intermetallic compound of composition Mg$_{17}$Al$_{12}$ and exhibits α-Mn-type cubic unit cell structure.[3–7] The precipitation of bcc β-Mg$_{17}$Al$_{12}$ from the parent hcp phase has two distinct and competitive modes of precipitation: continuous and discontinuous.[3–8] According to previous studies, around 80 pct of the precipitates are continuous precipitates, which can give a moderate increase in strength.[5,7,8] Therefore, it is of particular importance to understand the evolution of continuous precipitation of β-Mg$_{17}$Al$_{12}$ phase.

To this end, several experimental studies have been performed to gain comprehensive understanding of the morphology and structure of the β-Mg$_{17}$Al$_{12}$ phase, and its orientation relationship (OR) with the hcp matrix.[4,8–19] The results indicate that the continuous precipitate has a lath-shaped morphology, with the majority of precipitates forming with the habit plane parallel to the basal planes $(0001)_\alpha$ of the matrix.[4,6,8–11,17–19] These precipitates exhibit a near-Burgers OR with the matrix: $(0001)_\alpha||(110)_\beta$, $[1\bar{2}10]_\alpha||[1\bar{1}1]_\beta$.[8–11] The β precipitate phase has 12 variants. Due to symmetry, six groups, each having two variants, are related by about 60-deg rotation with respect to each other.[4,6] However, the morphology of the β-Mg$_{17}$Al$_{12}$ phase in three-dimensional (3D) space has not been well characterized yet. Furthermore, the mechanism underlying the evolution of precipitate mor-

GUOMIN HAN, Ph.D. Candidate, and ZHIQIANG HAN, Associate Professor, are with the Key Laboratory for Advanced Materials Processing Technology (Ministry of Education), School of Materials Science and Engineering, Tsinghua University, Beijing 100084, P.R. China. Contact e-mail: zqhan@tsinghua.edu.cn ALAN A. LUO, Professor, is with the Department of Materials Science and Engineering, and Department of Integrated Systems Engineering, College of Engineering, The Ohio State University, Columbus, OH 43210. BAICHENG LIU, Professor, is with the Key Laboratory for Advanced Materials Processing Technology (Ministry of Education), School of Materials Science and Engineering, Tsinghua University, and also with the Key Laboratory of Automotive Safety and Energy, Department of Automotive Engineering, Tsinghua University.
Manuscript submitted July 16, 2014.
Article published online December 4, 2014

phology cannot be completely revealed solely from experimental observations.

Phase-field simulation based on thermodynamic driving force and ordering potential is considered to be a powerful tool for modeling the morphology evolution of precipitates in two-dimensional (2D) and 3D space. In addition, it facilitates the understanding of the effects of various physical factors, such as interface anisotropy and elastic strain energy, on controlling the morphological evolution of precipitates. For example, Li et al. used 2D phase-field method to analyze the effect of elastic strain energy on the precipitation of θ' phase in Al-Cu alloy and morphological evolution of $Ti_{11}Ni_{14}$ precipitates in Ti-Ni alloys under an applied stress.[20,21] Similarly, Vaithyanathan et al.[22,23] studied the coarsening kinetics of δ'-Al_3Li precipitates by using 2D and 3D phase-field simulations. Moreover, they performed 2D multiscale modeling of θ' precipitation in Al-Cu binary alloys using phase-field method and analyzed the effects of interface anisotropy and elastic strain energy on the precipitation. Zhu et al.[24] investigated the coarsening kinetics of γ' precipitates in binary Ni-Al alloy using 3D phase-field model. Wen et al.[25] simulated the lamellar structure formation of γ phase in Ti-Al alloys using 3D phase-field model. More recently, Shi et al. analyzed the equilibrium shape and variant selection of α precipitates in Ti alloys using the 3D model.[26,27] Furthermore, for modeling the martensitic transformation, 2D or 3D phase-field simulations are being widely used for analyzing the effects of elastic field, external load, plasticity, and dilatation in single and polycrystalline materials and ceramic materials.[28–33]

Recently, there has been increased interest on the understanding of precipitation transformation in Mg alloys using phase-field model. The modeling of precipitation kinetics in AZ91 alloy started rather recently, following the pioneering studies of Li et al.[34] using 2D phase-field model and Wang et al.[35] using 3D model. Gao et al.[36] simulated the precipitation of β_1 phase in Mg-Y-Nd alloy using 2D phase-field model and discussed the effect of elastic strain energy on the precipitation. Meanwhile, Liu et al.[37] studied the effects of interface anisotropy and elastic strain energy on the morphology of β' precipitates in binary Mg-Y and Mg-Gd alloys using 2D phase-field simulation. In our previous study reported elsewhere, we investigated the effects of interface anisotropy and elastic strain energy on the morphology of the single- and multivariant β precipitates in Mg-Al-based alloy using 2D phase-field model.[38,39]

The phase-field simulations are highly successful in predicting the morphology evolution of precipitates in Mg alloys and many other materials, and facilitate fundamental understanding of the effects of various physical factors on morphology control. Nevertheless, most existing phase-field simulations are implemented in two dimensions. Therefore, extensive efforts should still be devoted for developing 3D phase-field model for a better understanding of the precipitation transformation, such as nucleation and morphology evolution of precipitates in 3D space. Especially in case of Mg-Al-

based alloys, there is a critical need for the 3D phase-field modeling of precipitation, as the effects of elastic interaction on nucleation are still unclear. Also related studies on the modulation of interface anisotropy and elastic strain energy to achieve adept control of the 3D morphology of precipitates, thereby enhancing the strength of Mg-Al alloy, have not been reported. In simple terms, there is no clear understanding or demonstration of alloy strengthening via precise control of the microstructural design. Therefore, both from fundamental and application standpoints, modeling the precipitation of Mg-Al system in 3D space is of great significance.

In this study, we have developed a 3D phase-field model to simulate the morphological evolution of precipitate phase in Mg-Al alloy, simultaneously considering the effects of both interface anisotropy and elastic strain energy. The developed model has been validated through experimental observations using combined techniques of atomic force microscopy (AFM) and transmission electron microscopy (TEM). Experimental observations provided valuable information on the morphology of the precipitate on basal and prism plane, especially the surface profile of the precipitate in 3D space, which correlate well with the simulation results. Further, discussions on the effects of anisotropic elastic interaction on subsequent nucleation near a pre-existing precipitate were conducted, which was supported by the experimental observations during aging processing in AZ91 alloy. The influences of interface anisotropy and elastic strain energy on the thickness of β-$Mg_{17}Al_{12}$ precipitate were elucidated by 3D simulation, and the inner connection of the microstructural design during precipitation with alloy strengthening was discussed. Finally, we have also proposed possible strategies for enhancing the strength of Mg-Al-based alloy.

The contents of the article are organized as follows: experimental methods are presented in Section II, followed by an elaborate description of the phase-field model, including chemical free energy calculation, elastic strain energy calculation, and construction of anisotropy of interfacial energy and interface mobility coefficient, in Section III. Experimental and simulation results are provided in Section IV, together with their implications. The major findings are summarized in Section V.

II. EXPERIMENTAL METHODS

Ingots of commercial AZ91 alloy were melted under protective atmosphere of nitrogen gas and sulfur hexafluoride. Subsequently, the molten alloy was cast in a steel mold, which was preheated to 523 K (250 °C), with a pressure of about 70 MPa. The typical composition of such a casting is shown in Table I.

The casting was cut into small pieces and heat treated at 686 K (413 °C) for 24 hour in order to achieve dissolution of eutectic β-$Mg_{17}Al_{12}$ phase and homogeneity of Al. These small pieces were embedded in MgO powder to prevent the rapid oxidation of experimental

Table I. Chemical Composition of the Experimental Mg Alloy (Weight Percentage)

Al	Zn	Mn	Si	Fe	Cu	Ni	Mg
8.91	0.763	0.257	0.0099	0.0033	0.001	0.0008	balance

Mg alloy during the solid solution process. After solid solution processing, the samples were quenched by plunging into water at 323 K (50 °C). This was done to avoid the cracking of samples under chilling conditions. Subsequently, the samples were aged at 573 K (300 °C) for 2 hour, followed by natural cooling in air. The solution-treated and aged samples were cut into thin bars of thickness 1 mm for TEM, and small cylindrical samples of diameter 8 mm and height 5 mm for AFM.

Prior to TEM, the 1-mm-thin bars were polished down to 0.2-mm-thin foils. Several disks of diameter 3 mm were punched from the thin foils for subsequent electropolishing. The disk specimens were polished in an electrolyte consisting of 5 vol pct perchloric acid and 95 vol pct ethanol at 243 K (−30 °C) and applied voltage of 25 V. TEM was performed on a FEI tecnai G20 electron microscopy.

The cylindrical specimens for AFM were mechanically ground with diamond abrasive paper up to 2000 grit, followed by polishing with napless polishing cloths loaded with a polycrystalline diamond paste of 0.5 μm grit, in order to obtain a mirror finish for AFM characterization. After polishing, the samples were immersed for about 10 seconds in an acid solution of 4 vol pct nitric acid and 96 vol pct ethanol. After chemical etching, AFM measurements were performed at room temperature in air. A maximum dimension of 5.0 × 5.0 μm^2 was used in the tapping mode for studying the surface profile of precipitates in three dimensions.

In this article, a term called the probability of tiny particle occurrence is defined, which is the ratio of the quantity of precipitates with tiny particles near their ends to the total quantity of the precipitates. In order to count precipitates, about 60 different SEM views, each of which contains at least 100 precipitates, are selected, which is found adequate to obtain a stable result of the probability.

III. MODEL DESCRIPTION

In this study, simulations were performed on a single β-Mg$_{17}$Al$_{12}$ precipitate, which is embedded in the matrix phase parallel to the basal plane. To distinguish the precipitate and matrix phases in the simulated Mg-Al system, the precipitation microstructure was described using one nonconserved quantity (the structural order parameter η) and one conserved quantity (molar fraction of the solute Al atom c). The 3D phase-field model for precipitation is designed on the basis of the thermodynamic description of interfaces proposed by Kim et al.[40] as follows:

$$\frac{\partial \eta}{\partial t} = -M(\varphi_x, \varphi_y, \varphi_z)\frac{\delta F}{\delta \eta}, \quad [1]$$

$$\frac{\partial c}{\partial t} = \nabla \cdot \left(\frac{D(T)}{f_{cc}} \nabla(f_c) \right) \quad [2]$$

where t is the time; $M(\varphi_x, \varphi_y, \varphi_z)$ denotes the interface mobility coefficient, where φ_x, φ_y, and φ_z are the angles between the interface normal direction and x-, y-, and z-axes, respectively; F represents the total free energy of the system, including chemical free energy, gradient energy, and elastic strain energy; $D(T)$ is the solute diffusivity, where T is the absolute temperature, and for simplicity, assume that $D(T) = D_0\exp(-Q/RT)$ only depends on the absolute temperature T,[6] where R is the universal gas constant, and the parameters D_0 (pre-exponential for solute diffusion) and Q (activation energy for Al diffusion) can be also found in Reference 6. In addition, f_c and f_{cc} are the first- and second-order derivatives of the total energy density f with respect to concentration, respectively.

A. Chemical Free Energy Calculation

The total free energy F is given by

$$F(c, \eta, T) = \int_v \left[f(c, \eta, T) + \frac{\varepsilon^2(\varphi_x, \varphi_y, \varphi_z)}{2}(\nabla \eta)^2 \right] dv + E^{ela}$$

$$[3]$$

where $\varepsilon(\varphi_x, \varphi_y, \varphi_z)$ is the gradient energy coefficient related to interface anisotropy; and E^{ela} denotes the elastic strain energy.

The chemical free energy density f of the system can be written as[40]

$$f = h(\eta)f^\beta(c_\beta, T) + (1 - h(\eta))f^\alpha(c_\alpha, T) + wg(\eta) \quad [4]$$

where c_α and c_β are the molar fraction of Al atoms in the matrix α- and β-Mg$_{17}$Al$_{12}$ precipitate, respectively; $h(\eta)$ denotes a monotonic function varying from 0 to 1; $g(\eta)$ is the double-well potential; and w is the height of the double-well potential. $f^\alpha(c_\alpha, T)$ and $f^\beta(c_\beta, T)$ represent the chemical free energy densities of the matrix and precipitate, respectively, which can be obtained directly from the commercial thermodynamic database Thermo-Calc.[39,41,42] In this study, $h(\eta)$ and $g(\eta)$ are selected as

$$h(\eta) = 3\eta^2 - 2\eta^3, \quad [5]$$

$$g(\eta) = \eta^2(1 - \eta)^2 \quad [6]$$

In the simulation, the interface region was assumed to be a mixture of the precipitate and matrix with different

compositions, but with equal chemical potentials. The compositions c_α and c_β satisfy the following constrain conditions[40]:

$$c = (1 - h(\eta))c_\alpha + h(\eta)c_\beta, \qquad [7]$$

$$\frac{\partial f^\alpha(c_\alpha, T)}{\partial c_\alpha} = \frac{\partial f^\beta(c_\beta, T)}{\partial c_\beta} \qquad [8]$$

The above two equations were solved for c_α and c_β by adopting an iterative algorithm coupled with the thermodynamic database.[39]

B. Elastic Strain Energy Calculation

In an Mg-Al-based alloy, the precipitate phase β is an intermetallic compound with α-Mn-type bcc structure, while the matrix phase is a solid solution with hcp crystal structure.[3,6,7] This structural difference between the precipitate phase and matrix phase causes a misfit strain. The eigen-strain tensor matrix of the hcp→bcc precipitation transformation was calculated by defining a one-coordinate system, as shown in Figure 1, where $[11\bar{2}0]_\alpha$, $[\bar{1}100]_\alpha$, and $[0001]_\alpha$ are set as x-, y-, and z-axes, respectively. Experimental observations suggest that precipitates exhibit a near-Burgers OR with the matrix: $(0001)_\alpha || (110)_\beta$, $[1\bar{2}10]_\alpha || [1\bar{1}1]_\beta$. In Figure 1, the red lines constitute $(110)_\beta$ of the β precipitate, while the blue lines comprise $(0001)_\alpha$ of the matrix. During the precipitation transformation, the lattice of the hcp matrix must be changed to that of the bcc precipitate. According to the lattice correspondence relationship shown in Figure 1, the lattice deformation matrix changing the matrix lattice into the precipitate lattice can be written as follows[5]:

$$\begin{pmatrix} \frac{a_\beta\sqrt{3}-6a_\alpha}{6a_\alpha} & 0 & 0 \\ 0 & \frac{a_\beta\sqrt{11}-6\sqrt{3}a_\alpha}{6\sqrt{3}a_\alpha} & 0 \\ 0 & 0 & \frac{a_\beta\sqrt{2}-3c_\alpha}{3c_\alpha} \end{pmatrix} \qquad [9]$$

where a_α and c_α are the lattice parameters of the matrix with hcp structure and take the value of 0.321 and 0.521 nm, respectively[5]; a_β is the lattice parameter of the precipitate phase with bcc structure and takes the value of 1.056 nm.[6] Moreover, it is necessary to realize the Burgers OR by a rigid-body rotation of 5.26 deg, as shown in Figure 1. Thus, the eigen-strain tensor matrix of the precipitation transformation with Burgers OR can be obtained by a rotational transformation of the lattice deformation matrix and expressed as

$$\varepsilon_{ij}^0 = (R\,5.26\,°)^{\mathrm{T}} \begin{pmatrix} \frac{a_\beta\sqrt{3}-6a_\alpha}{6a_\alpha} & 0 & 0 \\ 0 & \frac{a_\beta\sqrt{11}-6\sqrt{3}a_\alpha}{6\sqrt{3}a_\alpha} & 0 \\ 0 & 0 & \frac{a_\beta\sqrt{2}-3c_\alpha}{3c_\alpha} \end{pmatrix} (R\,5.26\,°)$$
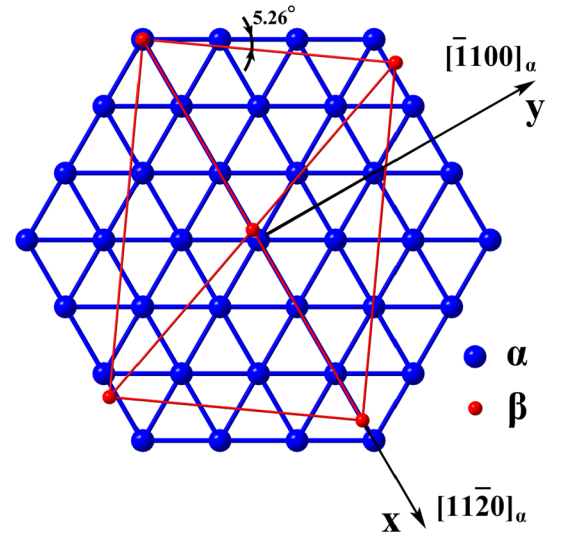
$$[10]$$

Fig. 1—Schematic diagram of hcp α-phase matrix lattice transformation to β precipitate lattice.

where ε_{ij}^0 is the eigen-strain tensor of precipitation transformation; and (R 5.26 deg) is the matrix of rigid-body rotation transformation and is defined as

$$(R\,5.26\,°) = \begin{pmatrix} \cos 5.26\,° & \sin 5.26\,° & 0 \\ -\sin 5.26\,° & \cos 5.26\,° & 0 \\ 0 & 0 & 1 \end{pmatrix} \qquad [11]$$

where (R 5.26 deg)$^{\mathrm{T}}$ is the transpose of (R 5.26 deg). Thus, the local stress-free transformation strain can be given by

$$\varepsilon_{ij}^0(r) = \varepsilon_{ij}^0 \eta^2 \qquad [12]$$

where η^2 is the so-called shape function, defined as 1 in the precipitate and 0 in the matrix. The final expression of the elastic strain energy E^{ela} can be written as follows on the basis of Khachaturyan's elastic strain theory[43]:

$$E^{\mathrm{ela}} = \frac{1}{2} \int \frac{d^3\vec{g}}{(2\pi)^3} B(\vec{n}) \{\eta^2\}_{\vec{g}} \{\eta^2\}_{\vec{g}}^*, \qquad [13]$$

$$B(\vec{n}) = \left[C_{ijkl}\varepsilon_{ij}^0\varepsilon_{kl}^0 - n_i\sigma_{ij}^0\Omega_{jk}(\vec{n})\sigma_{kl}^0 n_l \right] \qquad [14]$$

where $\vec{g}$ is a vector, and $\vec{n} = \frac{\vec{g}}{|\vec{g}|}$ is its corresponding unit vector in Fourier space. $\{\eta_p^2\}_{\vec{g}}$ denotes Fourier transform of η_p^2, and $\{\eta_q^2\}_{\vec{g}}^*$ denotes the complex conjugate of $\{\eta_q^2\}_{\vec{g}}$. $\Omega_{jk}(\vec{n})$ represents the reverse matrix of $\Omega_{jk}^{-1}(\vec{g}) = n_i C_{ijkl} n_l$. C_{ijkl} is the elastic modulus tensor. For numerical computation, we assumed that the modulus of the precipitate is the same as that of the matrix.[39] The components of the elastic modulus tensor are as follows: $C_{11} = 58$ GPa, $C_{12} = 25$ GPa, $C_{13} = 20.8$ GPa, $C_{33} = 61.2$ GPa, and $C_{44} = 16.6$ GPa.[34,39,44]

C. Construction of Anisotropy in Interfacial Energy and Interface Mobility Coefficient

A great majority of precipitation phase transformations in alloys occur by the growth of a new precipitate phase from the matrix. Therefore, the precipitate/matrix interfaces including the coherent, semicoherent, and noncoherent interfaces play an important role in determining the morphological evolution of the precipitate phase. The interfacial energy usually varies with different types of interface structure in phase transformation. The difference in interfacial energies results in the interface anisotropy for the growth of the new phase.

artificially. Hu et al.[48,49] defined the anisotropy of the interface mobility coefficient by a segmented function, similar to the definition of interfacial energy in 2D phase-field simulation of θ' precipitation in Al-Cu alloy. In the current study, we have artificially defined the anisotropy of interface mobility coefficient as a segmented function in 3D space, similar to that reported by Wang et al.,[35] where the interface mobility coefficient is incorporated as a function of the interface normal utilizing an artificial method to reflect the experimentally observed differences in interface kinetics, and the details are as follows:

$$M(\varphi_x, \varphi_y, \varphi_z) = M_0 \begin{cases} 1.0(\cos(\varphi_x))^2 + 0.2(\cos(\varphi_y))^2 + 0.002(\cos(\varphi_z))^2 & \frac{\pi}{2} - \varphi_0 \le \varphi_x \le \frac{\pi}{2} + \varphi_0 \\ 1 & \begin{cases} 0 \le \varphi_x < \frac{\pi}{2} - \varphi_0 \\ \frac{\pi}{2} + \varphi_0 < \varphi_x \le \pi \end{cases} \end{cases} \quad [18]$$

In general, it is critical to incorporate the interface anisotropy appropriately in the phase-field simulation of phase transformation. For instance, McFadden et al.[45] studied the incorporation of interfacial energy anisotropy in phase-field model for the solidification of a pure material. Similarly, Kazaryan et al.[46,47] introduced the interfacial energy anisotropy into phase-field model by a continuous function and investigated the effect of interfacial energy anisotropy on grain growth. In this study, the interfaces between the precipitate and matrix are assumed to be in a near-coherency state. The interfacial energy anisotropy can be introduced as

$$\sigma = \sigma_1 + (\sigma_2 - \sigma_1)f(\varphi_x) \quad [15]$$

$$f(\varphi_x) = \begin{cases} \frac{\frac{\pi}{2} - \varphi_x}{\frac{\pi}{2}} & \left(0 \le \varphi_x \le \frac{\pi}{2}\right) \\ \frac{\varphi_x - \frac{\pi}{2}}{\frac{\pi}{2}} & \left(\frac{\pi}{2} < \varphi_x \le \pi\right) \end{cases} \quad [16]$$

$$\varphi_x = ar\cos\left(\frac{\frac{\partial \eta}{\partial x}}{|\nabla \eta|}\right), |\nabla \eta| = \sqrt{\left(\frac{\partial \eta}{\partial x}\right)^2 + \left(\frac{\partial \eta}{\partial y}\right)^2 + \left(\frac{\partial \eta}{\partial z}\right)^2}$$

$$[17]$$

where σ_1 and σ_2 are the interfacial energies at $\varphi_x = \pi/2$ and $\varphi_x = 0$, taking the value of 140 and 390 mJ/m^2 from first-principles, respectively.[34]

In the KKS (Kim, Kim, and Suzuki) phase-field model, the interface mobility coefficient is closely related to the interfacial energy. Therefore, the anisotropy of interfacial energy must trigger the anisotropy of interface mobility coefficient.[40] However, the relationship between the interface mobility coefficient and interfacial energy is not just a simple linear function. In general, the interface mobility coefficient is influenced by interface kinetic coefficient, the experimental data of which are not yet available. Therefore, the anisotropy of the interface mobility coefficient has to be defined

where M_0 is the interface mobility coefficient at $\varphi_x = 0$; and $\varphi_0 = \pi/200$ is chosen as a small angle, which implies that the top and bottom interfaces have a small mobility. Figure 2 shows the interface mobility coefficient in 3D space.

The anisotropy of the interfacial energy and the interface mobility coefficient in the phase-field model are defined artificially. Uncertainties arising from such definitions are possible, which is a limitation of the current model. However, it is a huge challenge to determine these energies experimentally. We have noticed that first-principles calculation has been employed to calculate the interfacial energy and the phase-field mobility data.[50] In addition, Wang et al.[35] and Hu et al.[48,49] defined the anisotropy of the interfacial energy and the interface mobility coefficient in their phase-field models and used experimental results to validate their definitions. In the current study, experimental results are compared with simulation results to validate the model.

IV. RESULTS AND DISCUSSION

A. 3D Morphology of β Precipitate in Mg-Al-Based Alloy

The morphological evolution and characteristics of the precipitate were simulated using the model developed in 3D space, and only a single precipitate variant was considered in this study. A $128 \times 128 \times 128$ uniform grid was employed to numerically discretize the phase-field equations. In the simulation, the nucleation stage was ignored. At the beginning, one round seed was placed as the precipitate nucleus in the simulation domain. The initial composition of the precipitate and the matrix were 0.4 (molar fraction) and 0.076, respectively. The temperature of the domain was assigned to be 573 K (300 °C).

The simulation results shown in Figure 3 correspond to the morphological evolution of single precipitate aged at 573 K (300 °C) for different times, where both the
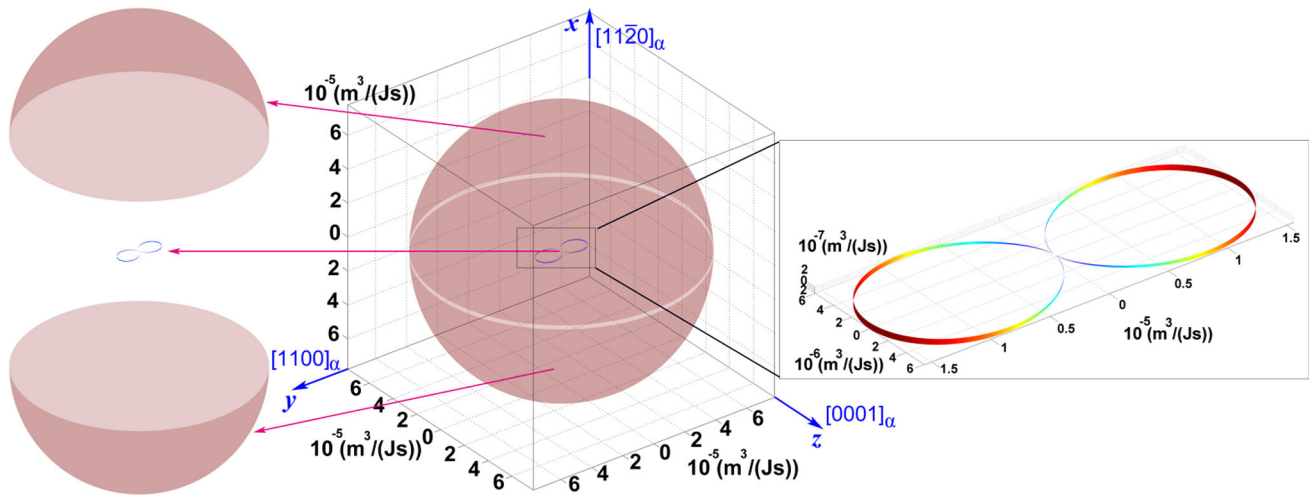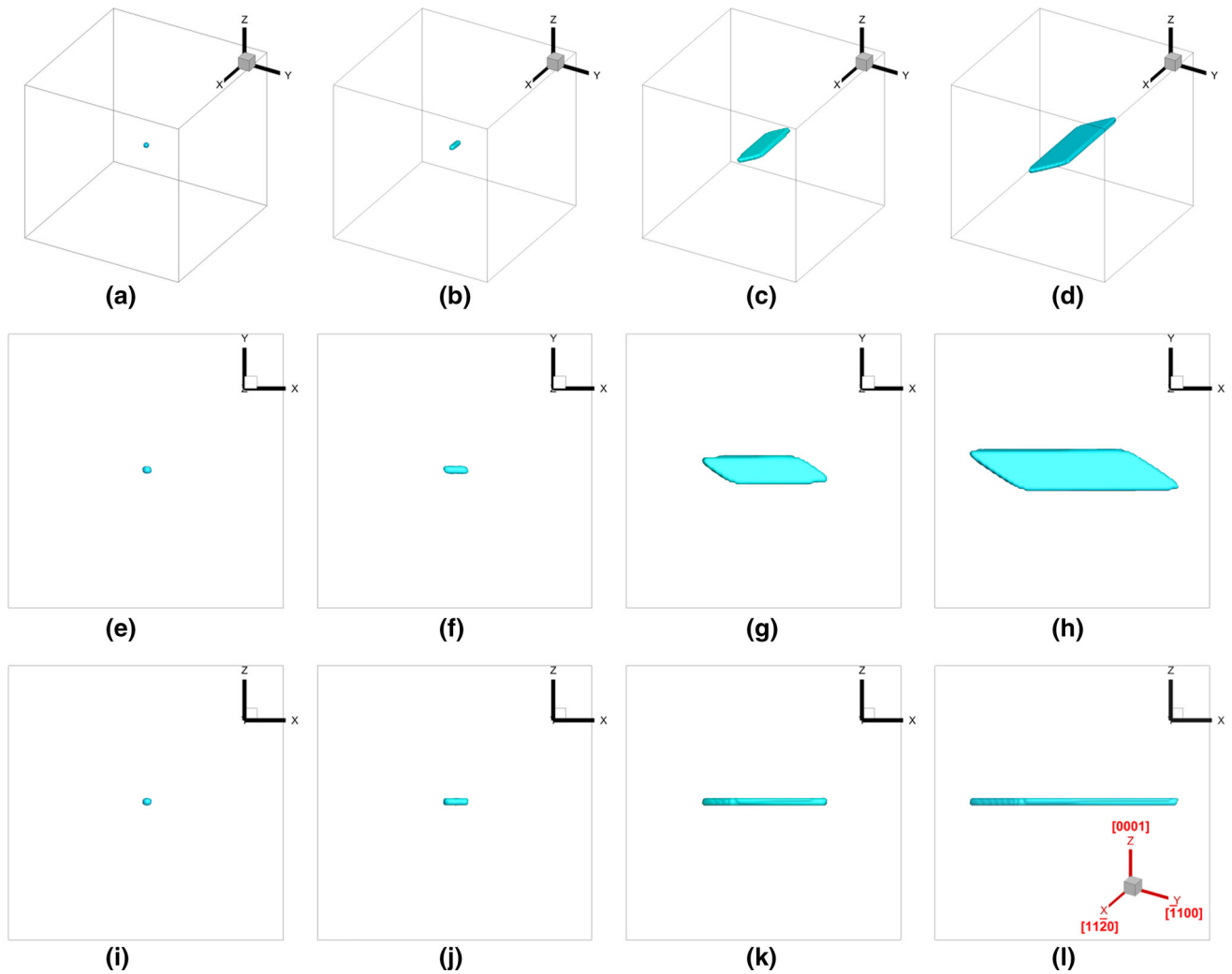
Fig. 2—The interface mobility coefficient in 3D space.

Fig. 3—Morphological evolution of β-Mg₁₇Al₁₂ precipitate in Mg-Al alloy aged at 573 K (300 °C), as determined from the 3D simulations: (a), (e), and (i) t = 5 s, ratio k = 0.59008; (b), (f), and (j) t = 25 s, ratio k = 0.83353; (c), (g), and (k) t = 150 s, ratio k = 1.62875; (d), (h), and (l) t = 250 s, ratio k = 2.17678; (e), (f), (g), and (h) are the morphologies on the basal plane (xy plane) of (a), (b), (c), and (d), respectively; (i), (j), (k), and (l) are the morphologies on the prism plane (xz plane) of (a), (b), (c), and (d), respectively. The size of the computational domain is 1280 × 1280 × 1280 nm³.
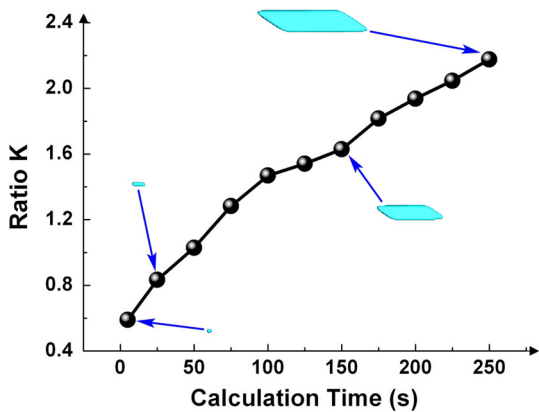
Fig. 4—Ratio k variation of elastic energy and interfacial energy with precipitate evolution and its effects on morphology of the precipitate.

interface anisotropy and elastic strain energy were considered. The blue-green areas in Figure 3 correspond to the precipitate, while the remaining blank areas represent the matrix. As is seen, the shape of the precipitate phase transforms as the simulation time proceeds. A near-spherical precipitate phase gradually evolves into a lath-shaped precipitate with lozenge ends. In general, the morphology of precipitate is determined by the interplay between interfacial energy and strain energy. In order to identify the effects of interfacial energy and elastic strain energy on precipitate morphology, a ratio k was defined as, $k = (e^{el}V)/(\sigma S)$, where e^{el} and σ are specific elastic strain energy and interfacial energy, respectively, and V and S are the total volume and surface area of precipitate, respectively. It is obvious that the effect of interfacial energy is dominant when ratio $k < 1$, as per the cases shown in Figures 3(a), (e), (i), (b), (f), and (j). It can be seen that the effect of interfacial energy is dominant when the precipitate is small. It may also represent the precipitate morphology in a system, wherein the elastic strain energy caused by the lattice misfit between the precipitate and matrix is almost negligible at this aging stage. The strong anisotropy of interfacial energy in 3D space (Eqs. [15], [16], and [17]) inhibits the growth of precipitate along y- and z-axes, and facilitates the formation of lath-shaped morphology, as shown in Figures 3(b), (f), and (j). With further growth of the precipitate phase, the ratio k starts to be greater than 1, as per the cases shown in Figures 3(c), (g), (k), (d), (h), and (l), and the elastic strain energy exerts an increasing influence on the morphological evolution of the precipitate. This could be attributed to the fact that the elastic strain energy increases with the precipitate volume.[20,23] From the point of view of throughout precipitate evolution, the ratio k is increasing, and the morphology characteristics of lozenge end of precipitate become more and more obvious (Figure 4). Figure 5 shows the morphological evolution of precipitate under different combination of energy. It is obvious the preferred growth orientations of the precipitate are different under different energy conditions. With the exertion of the elastic strain energy, the preferred growth orientation of the precipitate is

changed from PQ (Figure 5(c)) to UV (Figure 5(i)), thus forming the lozenge ends. It can also be seen that the preferred growth direction UV coordinates the direction PQ under only interfacial energy and the direction RS (Figure 5(f)) under only elastic strain energy. Consequently, the precipitate attains lozenge ends under the synergistic influence of interfacial energy and elastic strain energy, as shown in Figures 3(d), (h), and (l). It is worth noting that, during this precipitation transformation, the anisotropy of interfacial energy (Eqs. [15], [16], and [17]) is much stronger than that of elastic strain energy. The distributions of the interfacial energy between precipitate and matrix have large differences. Meanwhile, the anisotropy of elastic strain energy is not so strong due to the anisotropy factor (C_{33}/C_{11}) ≈ 1,[51] Therefore, the interfacial energy anisotropy will be responsible for forming a lath-shaped precipitate in total.

For comparison with the TEM observation results, the 3D simulation of the precipitate was projected onto 2D planes such as xy and xz planes. For better comparison, we also performed gray degree transformation of the image of the projected precipitate. In addition, for comparison with the AFM 3D surface plot, a special post-processing technique was employed to form a precipitate partially embedded in the matrix phase. All experimental results are shown in the right column of Figure 6. The morphology of precipitate at the basal plane has a lath shape with two lozenge ends, as evidenced from both in the simulated (Figure 6(a)) and TEM results (Figure 6(b)). On the other hand, the precipitate at prism plane has a thin lath shape, as shown in Figures 6(c) and (d). The simulated morphology of the precipitate projected onto a 2D plane agrees well with the TEM observations. For further comparison of the simulation with the experiment, we performed AFM for 3D surface plot of the precipitate. Figure 6(f) shows the 3D topographic images constructed from the surface height data obtained using AFM. The images show the surface profile of the precipitate in 3D. It can be seen that the 3D profile of the precipitate obtained by 3D phase-field simulation agrees well with that obtained by AFM. To quantitatively identify the characteristics of the 3D profile of the precipitate, the distribution of the surface height data along lines AB and CD can be shown, as presented in Figures 7(a), (b), and (c). Similar line scanning was conducted for the surface of simulation system for comparing with the AFM results (Figures 7(d), (e), and (f)). It can be clearly seen that the top surface of the precipitate is wide and flat, while the side surfaces are nearly perpendicular to the top surface; the two short and parallel sides constitute the two lozenge ends of the precipitate, which is in good agreement with the AFM observations. However, the tops of the curves in Figures 7(b) and (c) are just nearly linear, but not flat compared with Figures 7(e) and (f), which is mainly attributed to the fact that Figure 7(a) is just an approximate location of the base plane and may be lean to a certain angle with the base plane $(0001)_m$. As we know, the OR cannot be determined precisely during AFM observations compared with TEM observations.
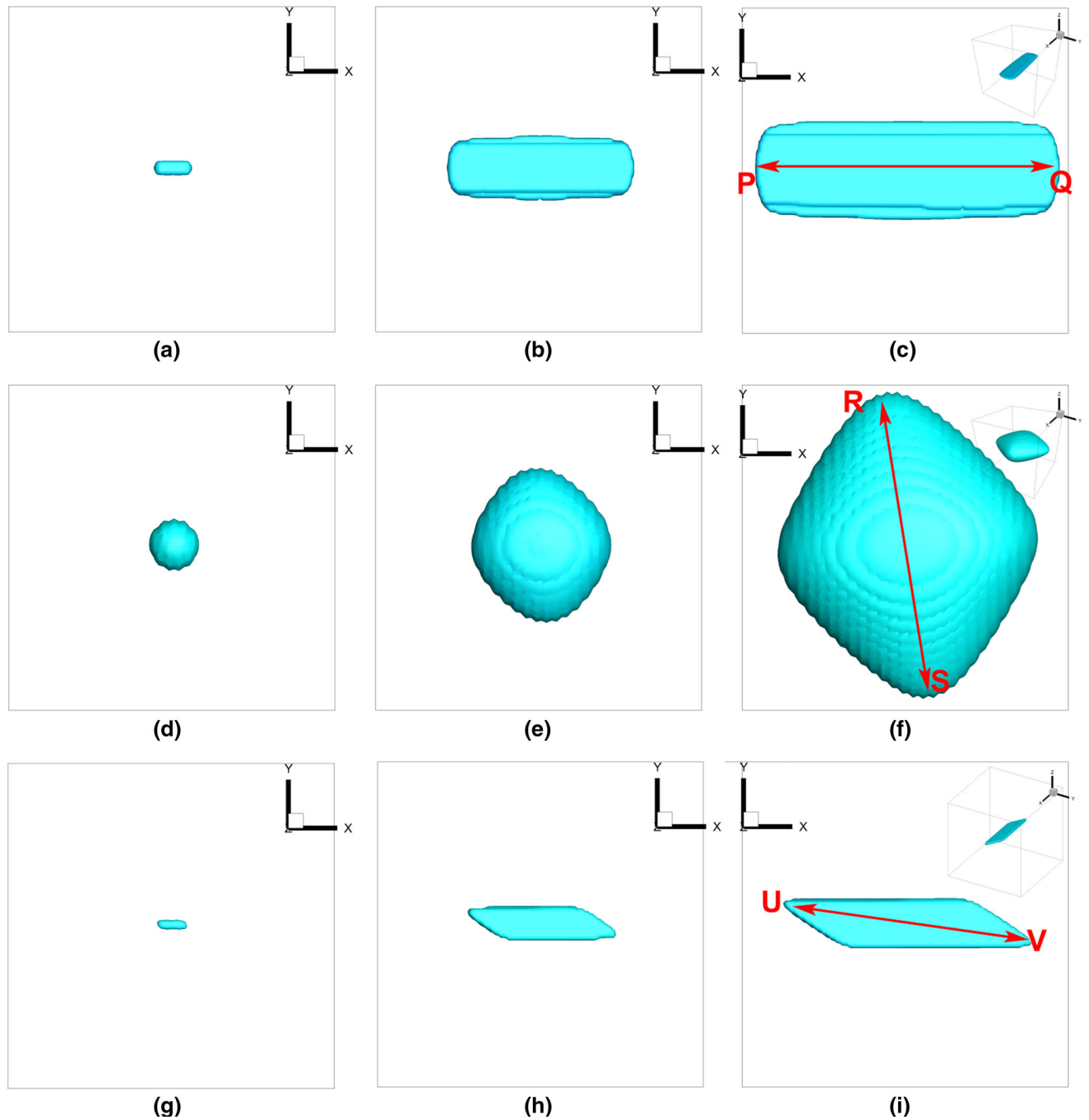
Fig. 5—Preferred growth orientation of β-Mg$_{17}$Al$_{12}$ precipitate, as determined from the 3D simulations: (a), (b), and (c) considering only the interfacial energy; (d), (e), and (f) considering only the elastic strain energy; (g), (h), and (i) considering both the interfacial energy and elastic strain energy. The size of the computational domain is 1280 × 1280 × 1280 nm^3.

So in our AFM observations, we can just probably determine the position of the base plane according to the morphological characteristics of precipitate.

B. Nucleation in a Medium with Elastic Strain Field

The TEM and SEM observations of the precipitate revealed an intriguing phenomenon. As shown in Figure 8, a tiny particle is located near one end of a mediate precipitate. However, this is not a unique phenomenon. For instance, the TEM image shown in[52] also shows the presence of a tiny particle near one end of a mediate precipitate. However, this phenomenon has not been emphasized or explained in the abovementioned reference. We believe that a fundamental understanding of this phenomenon would be of great scientific interest. It is speculated that this particle is related to some particular mechanism of nucleation, which may be responsible for dictating the location of the newly formed nucleus. Profound investigation of this
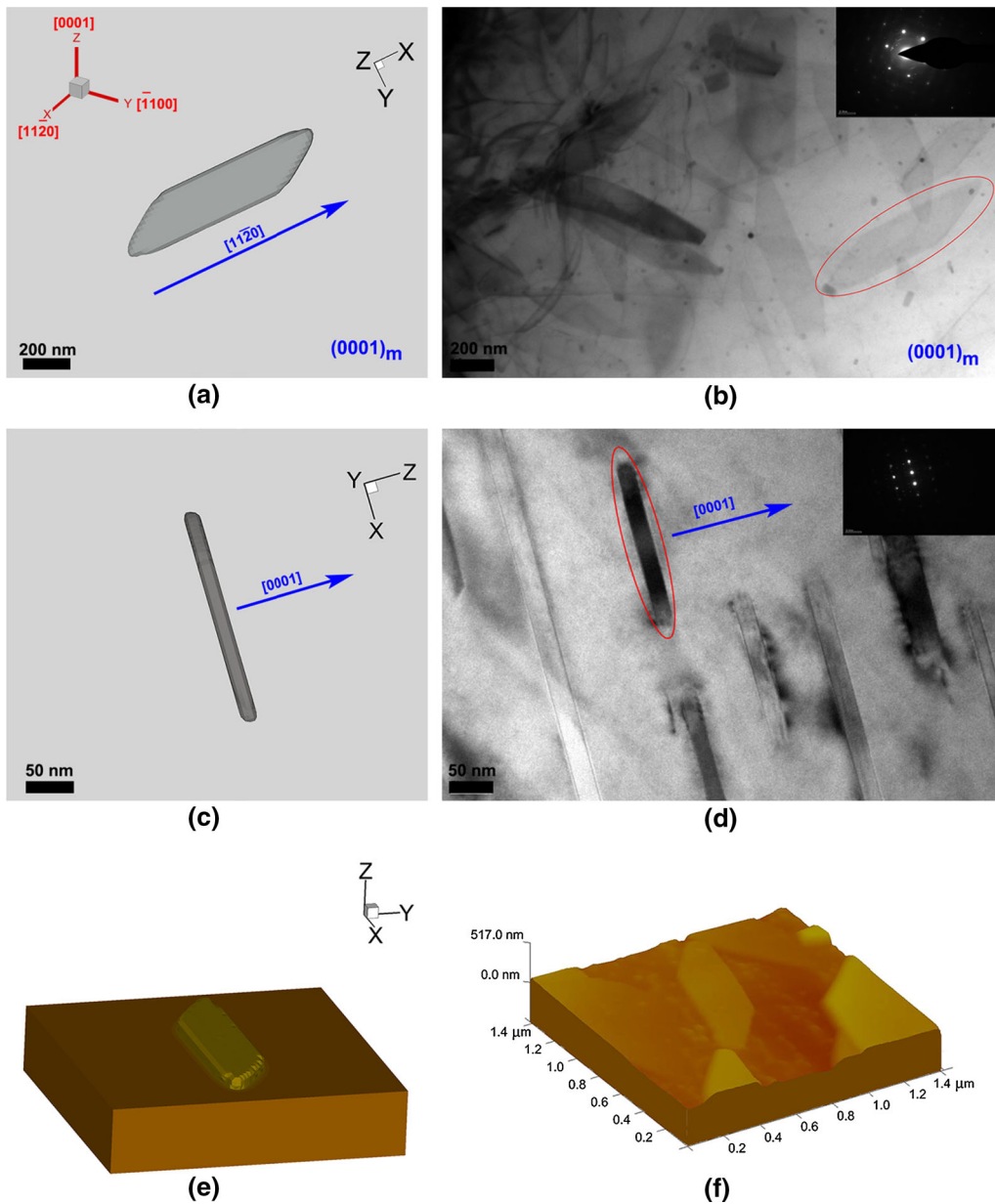
Fig. 6—Comparison of the morphology of a single β-Mg$_{17}$Al$_{12}$ precipitate obtained by simulations and experimental observations in a Mg-Al alloy aged at 573 K (300 °C): (*a*) and (*c*) the simulation results of precipitate morphology projected in 2D *xy* and *xz* planes (the basal and prism planes), respectively; (*e*) the simulation morphology of precipitate in 3D; (*b*) and (*d*) the TEM images of precipitate lying in basal and prism planes, respectively, for AZ91 alloy aged at 573 K (300 °C) for 2 h; (*f*) 3D surface plot of precipitate obtained by AFM in its topographic modes for AZ91 aged at 573 K (300 °C) for 2 h.

phenomenon was performed through systematic experiments, as shown in Table II. This phenomenon has also been observed in other samples under different treatment. The statistical probability of the occurrence of this phenomenon, which is defined as the number of precipitates with a tiny particle on one lozenge end divided by the total number of precipitates in the region of observation, was also calculated for the samples with different treatments. Due to the wide distribution range of the statistical data, several observation regions with approaching magnification were counted, as presented in Figure 9. It can be observed that the phenomenon is triggered with maximum probability in the mid-aging stage. It is speculated that these tiny particles could be new nuclei. During the early stage of aging, the size of all nuclei, including the newly formed nucleus, is close, while the pre-existing precipitate annexes the pro-nucleus due to coarsening at the later stage of aging. This speculation could be further substantiated from the energy-dispersive X-ray spectroscopic (EDS) results shown in Figure 10. According to the EDS analysis, the composition of the tiny particle in Figure 8 approaches that of the precipitate phase. The difference in compositions between the particles with near 38 pct
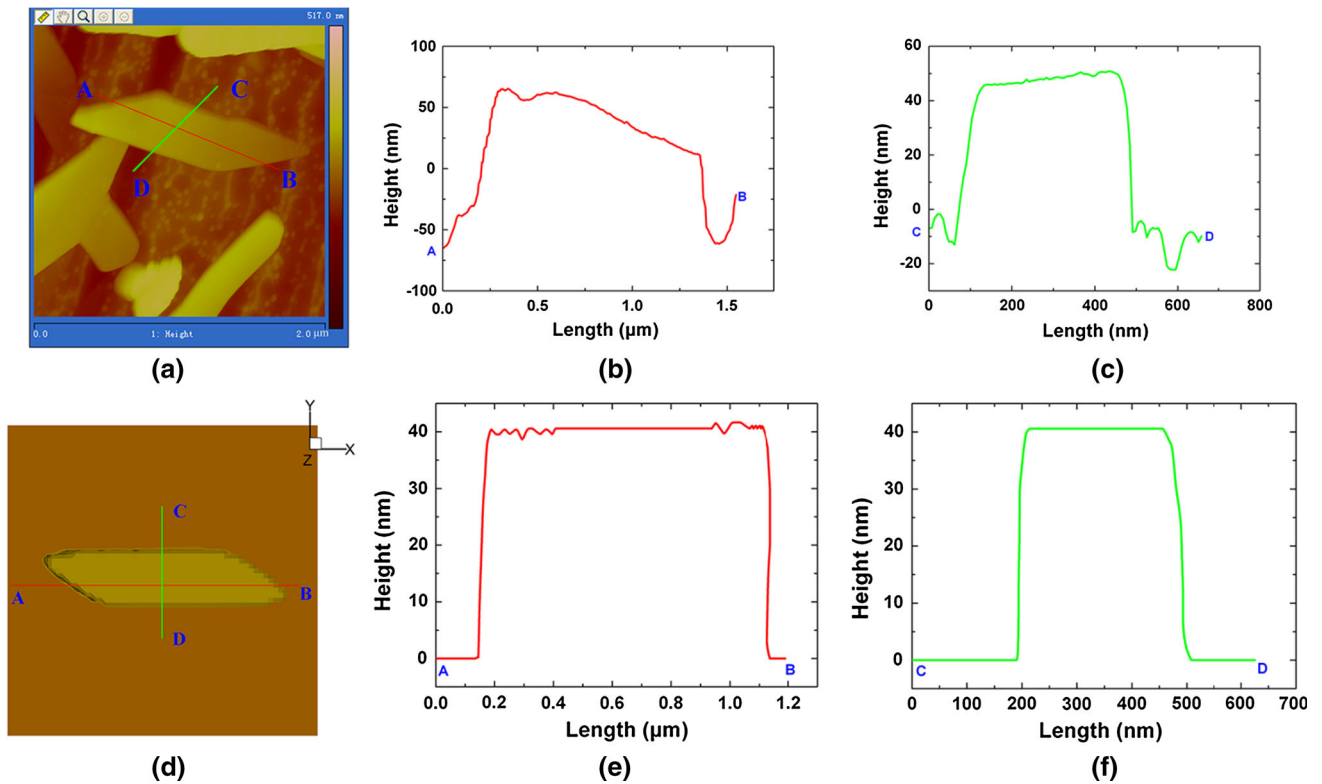
Fig. 7—Comparison of the 3D profiles of a single β-Mg₁₇Al₁₂ precipitate obtained by experimental observations and simulations in a Mg-Al alloy aged at 573 K (300 °C): (*a*), (*b*), and (*c*) the experimental AFM results for AZ91 aged at 573 K (300 °C) for 2 h; (*d*), (*e*), and (*f*) simulation results obtained using a 3D phase-field model.
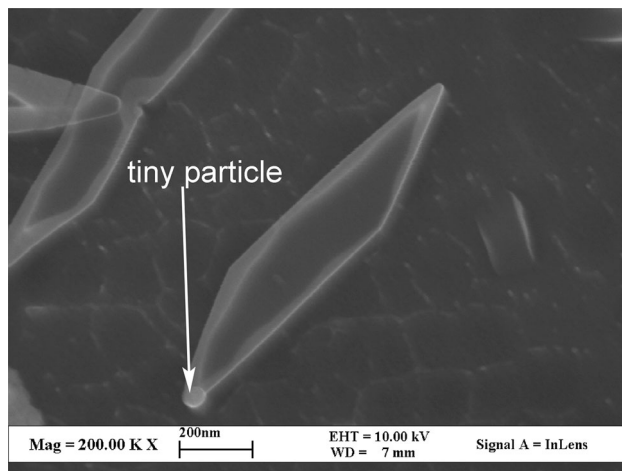

Fig. 8—Experimental observation of the tiny particle near one end of the precipitate using SEM in AZ91 aged at 573 K (300 °C) for 2 h.

(Al atomic fraction) and pre-existing precipitate with near 41 pct (Al atomic fraction) may be due to the limitation of the EDS analysis in itself, which has an excitation region radius of about 500 nm much larger than the particle size. Therefore, on the basis of the results, it can be concluded that the tiny particle is a newly formed nucleus that tends to form near the end of the pre-existing precipitate. Besides, it is difficult to clarify the OR between the tiny particle and the matrix.

Nevertheless, the reason for the origin of this unique nucleation phenomenon needs to be explored further.

Until now, several studies have investigated the phenomenon of nucleation in solid transformation by phase-field modeling. For instance, Zhang *et al*.[53,54] studied the effect of elastic strain energy on the nucleation of precipitation and predicted the shape of a critical nucleus. Similarly, Shen *et al*.[55,56] investigated the effect of pre-existing precipitate on the nucleation in Ni alloys. According to their study, the primary factor influencing the nucleation stage during precipitation transformation is the elastic strain energy. In general, the probability of nucleation is closely related to the driving force for nucleation, including the chemical free energy and elastic strain energy.[53–55] The chemical free energy can be measured on the free energy curve by the parallel line construction. It is uniform regardless of the position in a given system, while the elastic strain energy including the two parts of self-energy and interaction energy is not uniform in 3D space. The self-energy is always positive.[55,56] Accordingly, the interaction energy obviously affects the driving force for nucleation and the corresponding nucleation probability of location in 3D space. However, to the best of our knowledge, there are no studies on the nucleation during solid transformation in Mg-Al alloy using phase-field modeling. To this end, we performed phase-field simulation of Mg-Al alloy in an effort to explain the above-mentioned phenomenon.

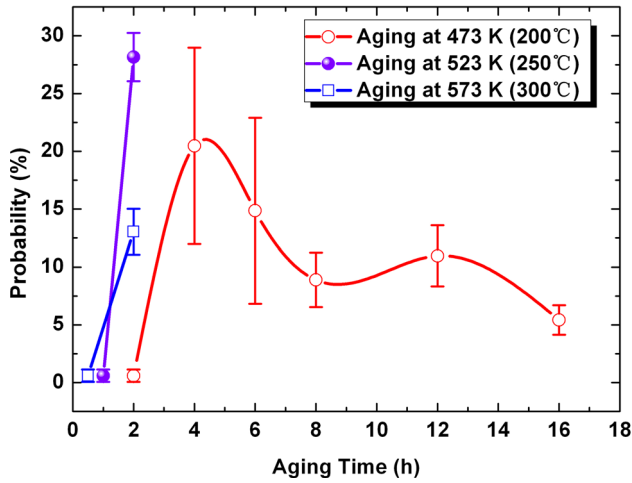|	SS Temperature [K (°C)]	SS Time (h)	Aging Temperature [K (°C)]	Aging Time (h)
1#	686 (413)	24	473 (200)	2
2#	686 (413)	24	473 (200)	4
3#	686 (413)	24	473 (200)	6
4#	686 (413)	24	473 (200)	8
5#	686 (413)	24	473 (200)	12
6#	686 (413)	24	473 (200)	16
7#	686 (413)	24	523 (250)	1
8#	686 (413)	24	523 (250)	2
9#	686 (413)	24	573 (300)	0.5
10#	686 (413)	24	573 (300)	2

Fig. 9—Probability of the occurrence of the proposed tiny particle near one end of the precipitate in AZ91 aged at different temperatures and times.
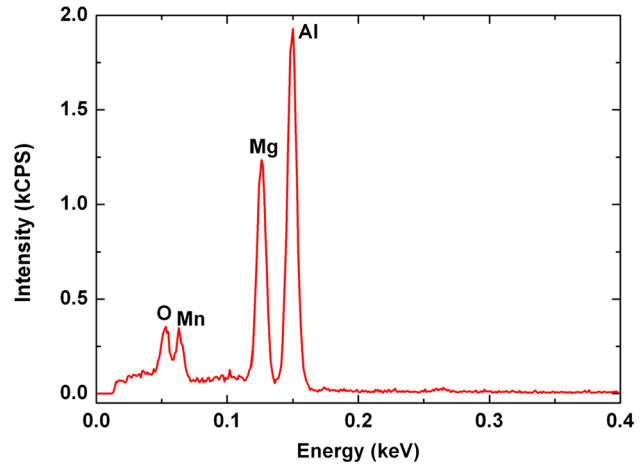

Fig. 10—EDS analysis of the composition of the tiny particle in Fig. 8 in AZ91 aged at 573 K (300 °C) for 2 h.

As previously analyzed, the nonuniform of the interaction energy would significantly affect the nucleation probability of location in 3D space compared with the uniform chemical free energy. So we must accurately determine the distribution of the interaction energy in 3D space. In the case study, the interaction energy per volume (ΔE_{int}^{el}) was calculated using the following formulation[53]:

$$\Delta E_{int}^{el} = (\eta_0 - \eta)\left\{ B\left(\bar{n}\right)\{\eta\}_{\bar{g}} \right\}_{\bar{x}} \qquad [19]$$

where η_0 is the equilibrium order parameter; $\{\eta\}_{\bar{g}}$ denotes the Fourier transform of η, and $\left\{ B\left(\bar{n}\right)\{\eta\}_{\bar{g}} \right\}_{\bar{x}}$ denotes the inverse Fourier transform of $\left\{ B\left(\bar{n}\right)\{\eta\}_{\bar{g}} \right\}$. In the phase-field modeling, the distribution of order parameter near a pre-existing precipitate was used as the input for Eq. [19]. Figure 11(a) shows the distribution of interaction energy in 3D space. The red area denotes the location with minimum values which tend to promote nucleation. In simple terms, the probability for the formation of new nucleus is maximum in the red area. Figure 11(b) shows the relative position of the newly formed nucleus and pre-existing precipitate. It can be clearly seen that

the new nucleus (blue) is indeed located near one lozenge end of the pre-existing precipitate (red), which is in good agreement with the above phenomenon (Figure 8). However, it is worth noting that the experimental observation of this phenomenon essentially suggests that the end of the pre-existing precipitate has large probability compared with other positions. This phenomenon does not necessarily occur during the aging process. Besides, because of the lack of precise information of orientation of the tiny particle, the simulation and analysis of the case study just provide a possible explanation for this phenomenon.

C. Increasing the Thickness of β Precipitate to Strengthen Mg-Al Alloys

It has been reported that the predominant OR between the continuous β precipitate and α-Mg matrix is the Burgers OR.[4–7] It has also been reported that only few precipitates have four other ORs: the Crawley OR,[4,9,11] Porter OR,[4,16] Gjömmes-Östrmoe OR,[17,57] and Potter OR.[7,17] These precipitates often lie nearly perpendicular to the basal plane of the matrix and have enhanced ability to block dislocation motion. Normally, in the alloy system with $(0001)_\alpha$ slip plane, those precipitates in the form of $[0001]_\alpha$ rods and those
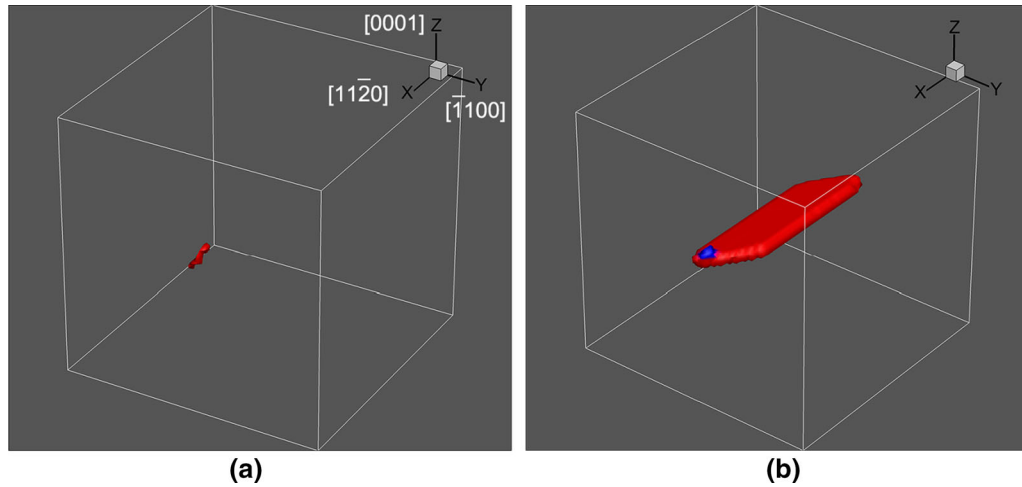
Fig. 11—Simulation results of the distribution of interaction energy and the location of newly formed nucleus near the pre-existing precipitate in AZ91 alloy. (*a*) Distribution of the minimum value of the interaction energy near a pre-existing precipitate and (*b*) the relative position of the newly formed nucleus and pre-existing precipitate in space.
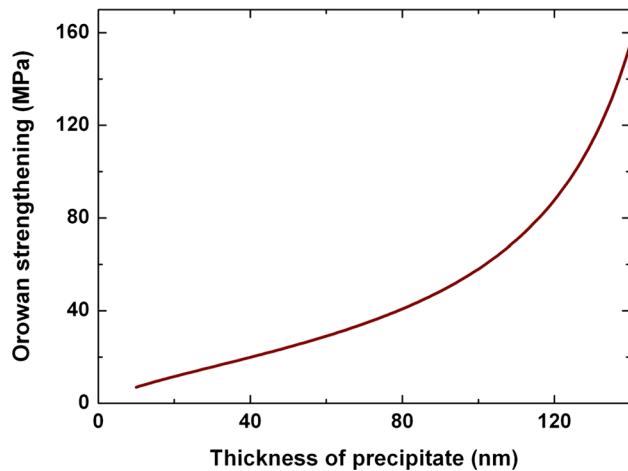

Fig. 12—The calculated Orowan strengthening as a function of thickness of precipitate estimated from Eqs. [20] and [21].

plate-shaped precipitates formed on prismatic planes of the matrix phase are the most effective for Orowan strengthening, and larger aspect ratio for these precipitates will offer higher densities of interfaces to hinder dislocation motion in $(0001)_\alpha$ plane, and hence better mechanical properties.[58] However, in the Mg-Al alloy system, a majority of precipitates are thin lath, which are formed on the basal plane $(0001)_\alpha$ of the matrix phase. For these precipitates, increasing the density of top and bottom surfaces is not very useful in blocking dislocation motion in $(0001)_\alpha$ plane, while increasing the density of side surfaces, *i.e.*, increasing the thickness of the precipitate, may be able to improve the strengthening effect to block gliding dislocations. According to Nie *et al.*,[7,58] the dislocation always bypasses the precipitates in Mg-Al alloy (AZ91). The contribution to strengthening, *i.e.*, Orowan strengthening, provided by the interactions between precipitates parallel to the basal

plane and dislocation has been investigated and can be approximated by the following equation[6,7]:

$$\sigma_p = \left(\frac{0.81 MGb}{2\pi(1-v)^{\frac{1}{2}}} \frac{1}{\lambda} \right) \ln \frac{d}{r_0} \qquad [20]$$

where M is the Taylor factor; G is the shear modulus of the matrix; b is the Burgers vector of the dislocation; v is Poisson's ratio; λ and d are the mean spacing and mean diameter of precipitates in the slip plane, respectively; and r_0 is the inner cut-off radius of the dislocations, which is approximately equal to b. The spacing of plate-like precipitates can be calculated by Eq. [21].[6]

$$\lambda = \frac{1}{\sqrt{N_V \cdot t}} - d \qquad [21]$$

where t is the precipitate thickness; and N_V is the number of particles per unit volume, where V is the volume of a single precipitate. Combining Eqs. [20] and [21], it is obvious that the Orowan strengthening would increase with the precipitate thickness as shown in Figure 12. Therefore, identifying strategies for increasing the precipitate thickness is of great significance, to allow strengthening the alloy and widening its application. In a nutshell, the increase in the precipitate thickness forms the critical issue for rational design of the alloy. In Section IV–A, it has been concluded that the morphology is determined by the combinational effects of interfacial energy and elastic strain energy. To further substantiate this conclusion, case studies were conducted to identify other factors that affect the precipitate thickness using different combinations of interfacial energy and elastic strain energy. The anisotropy of interface mobility coefficient is triggered by the anisotropy of interfacial energy in all the following cases.

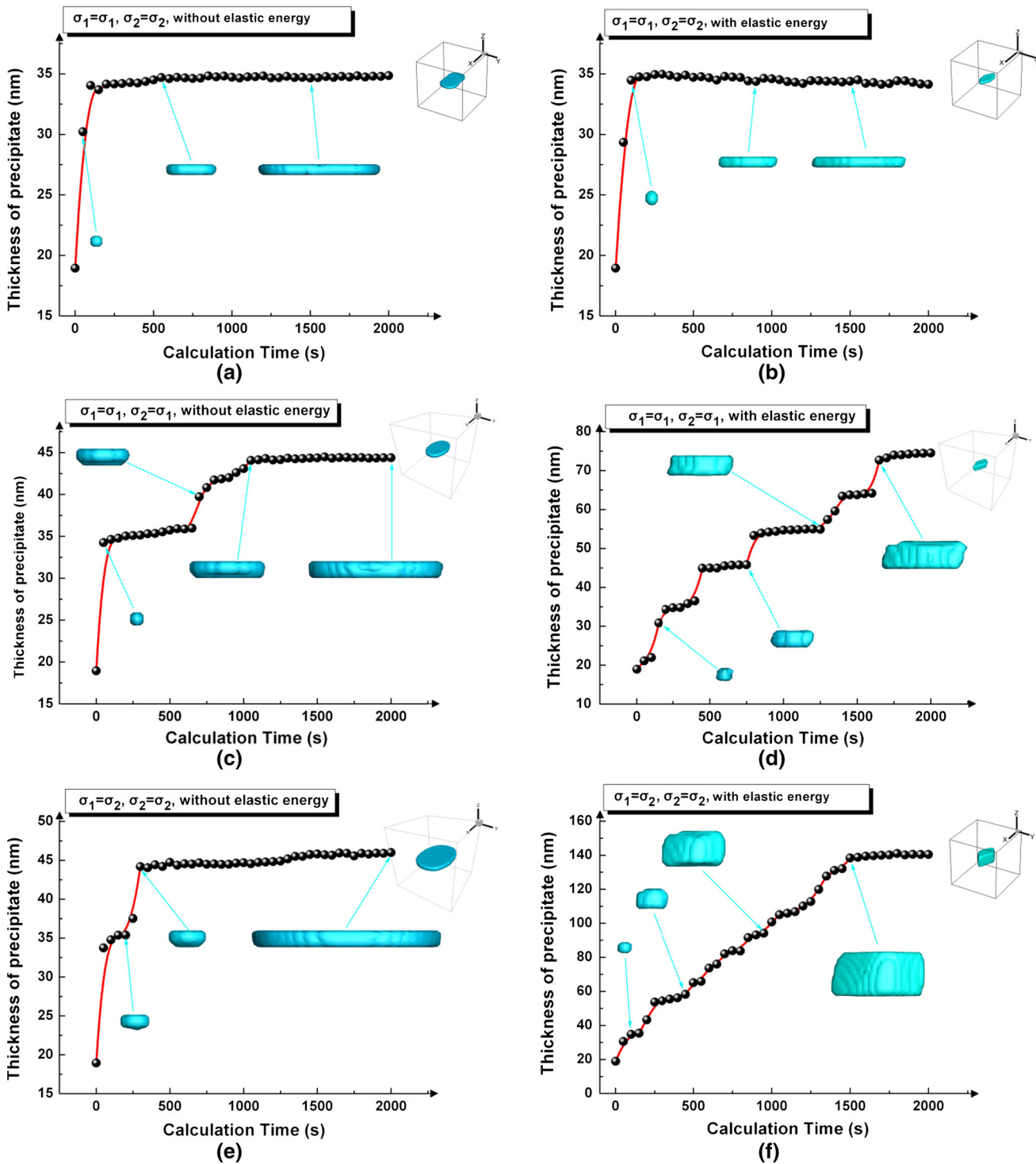The simulation results shown in Figure 13 reveal the precipitate thickness under different combinations of

Fig. 13—Simulation results of the precipitate thickness under different combinations of interfacial energy and elastic energy in AZ91 aged at 573 K (300 °C). (a) and (b) interfacial energy $\sigma_1 = \sigma_1$, $\sigma_2 = \sigma_2$ without and with elastic energy, respectively; (c) and (d) interfacial energy $\sigma_1 = \sigma_1$, $\sigma_2 = \sigma_1$ without and with elastic energy, respectively; (e) and (f) interfacial energy $\sigma_1 = \sigma_2$, $\sigma_2 = \sigma_2$ without and with elastic energy, respectively.

interfacial energy and elastic energy. The aging temperature was fixed as 573 K (300 °C). The case with the condition of interfacial energy, i.e., $\sigma_1 = \sigma_1$, $\sigma_2 = \sigma_2$ without elastic strain energy, is shown in Figure 13(a). As is seen, the precipitate thickness is small and remains

almost unchanged with aging. Even after including the effect of elastic strain energy, the results of the simulation (Figure 13(b)) is almost the same as those of Figure 13(a). Furthermore, Figures 13(c) and (e) shows the simulation results without elastic strain energy but

under the different conditions of interfacial energy, *i.e.*, $\sigma_1 = \sigma_1$, $\sigma_2 = \sigma_1$ and $\sigma_1 = \sigma_2$, $\sigma_2 = \sigma_2$, respectively. The four cases verify that the above combination of interfacial energy and elastic energy has no obvious effect in increasing the precipitate thickness. Therefore, the fifth and sixth cases were performed to identify the appropriate combination of interfacial energy and elastic energy. In these two cases, we all considered the effects of the elastic strain energy, assuming the interfacial energy to be $\sigma_1 = \sigma_1$, $\sigma_2 = \sigma_1$ and $\sigma_1 = \sigma_2$, $\sigma_2 = \sigma_2$, respectively. The simulation results of the two cases shown in Figures 13(d) and (f) indicate that the precipitate thickness increases at a certain degree, and the case of Figure 13(f) increases significantly with about twice the maximum thickness of Figure 13(d).

As previously mentioned, the effects of interfacial energy and elastic strain energy in different directions in space would be different, thus forming different preferred growth orientation. One can readily see from Figures 13(a), (c), and (e) that the strong interfacial energy anisotropy would inhibit the growth of precipitate in z direction. The precipitate thicknesses in the two cases with isotropic interfacial energy (Figures 13(c) and (e)) are slightly larger than that with strong interfacial energy anisotropy (Figure 13(a)). Furthermore, it can be seen from Figures 13(d) and (f) that the elastic strain energy can promote the growth of precipitate in *z* direction even though the promotion in *z* direction is much weaker than that in RS (Figure 5(f)) direction. However, this effects of the elastic strain energy in promoting growth would be offset by strong interfacial energy anisotropy, as shown in Figure 13(b). Besides, the comparison of Figures 13(d) and (f) shows that the larger the value of interfacial energy, the larger the thickness of the precipitate under isotropic interfacial energy. Therefore, the potential strategy of increasing the precipitate thickness and thereby strengthening the alloy is to make the interfacial energy as approaching or isotropic as possible. So, a different outlook on the synergistic effects of interfacial energy and elastic strain energy on the precipitate thickness as an effective way to strengthen the alloy may facilitate better alloy design.

It is reported that adding Si or Sc element changes the precipitate/matrix interfacial energy in Al-Cu alloys.[59,60] However, we have not seen such report for Mg-Al system. Although we are not aware of any possible strategies, we believe that a similar possibility to modify the precipitate/matrix interfacial energy may also exist in Mg-Al alloy.

V. CONCLUSIONS

1. A 3D phase-field model has been developed to simulate the single β-$Mg_{17}Al_{12}$ phase precipitation in Mg-Al based alloys, considering the synergistic effects of elastic strain energy, anisotropy of interfacial energy, and anisotropy of interface mobility coefficient. The morphological evolution has been studied on the basis of the effects of interface anisotropy and elastic strain energy on the morphology of a single β-$Mg_{17}Al_{12}$ precipitate. The morphology of the precipitate in 3D space was analyzed by both AFM and TEM. The results indicate that a spherical precipitate phase gradually evolves into a lath-shaped precipitate with lozenge ends with aging, and this morphology characteristic is in good agreement with 2D TEM and 3D AFM surface profile observations.

2. The distribution of elastic interaction energy near a pre-existing precipitate was calculated by 3D phase-field simulation. The effects of anisotropic elastic interaction on subsequent nucleation of β phase near a pre-existing precipitate were also investigated. The results show that the anisotropic elastic interaction can exert a significant effect on the location of subsequent nucleation and promote the formation of the new nucleus near the lozenge ends of the pre-existing precipitate, which are in good agreement with the experimental observations.

3. According to the case studies using the developed 3D phase-field model, different combinations of interface anisotropy and elastic strain energy have an obvious effect on the thickness of β-$Mg_{17}Al_{12}$ precipitate. Therefore, one possible strategy to increase the thickness, and thereby strengthen the alloy, is to make the interfacial energy equal or as approaching or isotropic as possible. Such an approach is expected to improve the alloy design in Mg-Al-based alloys.

REFERENCES

1. B.L. Mordike and T. Ebert: *Mater. Sci. Eng., A*, 2001, vol. 302, pp. 37–45.
2. A.A. Luo: *J. Magnes. Alloys*, 2013, vol. 1, pp. 2–22.
3. A.A. Luo, C. Zhang, and A.K. Sachdev: *Scripta Mater.*, 2012, vol. 66, pp. 491–94.
4. S. Celotto: *Acta Mater.*, 2000, vol. 48, pp. 1775–87.
5. K.N. Braszczynska-Malik: *Magnesium Alloys-Design, Processing and Properties*, 1st ed., InTech Press, Croatia, 2011, pp. 95–112.
6. C.R. Hutchinson, J.F. Nie, and S. Gorsse: *Metall. Mater. Trans. A*, 2005, vol. 36A, pp. 2093–2105.

7. J.F. Nie: *Metall. Mater. Trans. A*, 2012, vol. 43A, pp. 3891–3939.
8. J.B. Clark: *Acta Metall.*, 1968, vol. 16, pp. 141–52.
9. A.F. Crawley and B. Lagowski: *Metall. Trans.*, 1974, vol. 5, pp. 949–51.
10. J. Gjömmes and T. Östrmoe: *Z. Metallkd.*, 1970, vol. 31, pp. 604–06.
11. A.F. Crawley and K.S. Milliken: *Acta Metall.*, 1974, vol. 22, pp. 557–62.
12. D.A. Porter and J.W. Edington: *Proc. R. Soc. A*, 1977, vol. 358, pp. 335–50.
13. D. Duly and Y. Brechet: *Acta Metall. Mater.*, 1994, vol. 42, pp. 3035–43.
14. D. Duly, M.C. Cheynet, and Y. Brechet: *Acta Metall. Mater.*, 1994, vol. 42, pp. 3843–54.
15. D. Duly, J.P. Simon, and Y. Brechet: *Acta Metall. Mater.*, 1995, vol. 43, pp. 101–06.
16. D. Duly, W.Z. Zhang, and M. Audier: *Phil. Mag. A*, 1995, vol. 71, pp. 187–204.
17. J.F. Nie, X.L. Xiao, C.P. Luo, and B.C. Muddle: *Micron.*, 2001, vol. 32, pp. 857–63.
18. J.F. Nie: *Acta Mater.*, 2004, vol. 52, pp. 795–807.
19. J.F. Nie: *Metall. Mater. Trans. A*, 2006, vol. 37A, pp. 841–49.
20. D.Y. Li and L.Q. Chen: *Acta Metall. Mater.*, 1998, vol. 46, pp. 2573–85.
21. D.Y. Li and L.Q. Chen: *Acta Metall. Mater.*, 1998, vol. 46, pp. 639–49.
22. V. Vaithyanathan and L.Q. Chen: *Scripta Mater.*, 2000, vol. 42, pp. 967–73.
23. V. Vaithyanathan, C. Wolverton, and L.Q. Chen: *Phys. Rev. Lett.*, 2002, vol. 88, pp. 125503–4.
24. J.Z. Zhu, T. Wang, A.J. Ardell, S.H. Zhou, Z.K. Liu, and L.Q. Chen: *Acta Mater.*, 2004, vol. 52, pp. 2837–45.
25. Y.H. Wen, L.Q. Chen, P.M. Hazzledine, and Y. Wang: *Acta Mater.*, 2001, vol. 49, pp. 2341–53.
26. R. Shi, N. Ma, and Y. Wang: *Acta Mater.*, 2012, vol. 60, pp. 4172–84.
27. R. Shi and Y. Wang: *Acta Mater.*, 2013, vol. 61, pp. 6006–24.
28. W. Zhang, Y.M. Jin, and A.G. Khachaturyan: *Acta Mater.*, 2007, vol. 55, pp. 565–74.
29. H.K. Yeddu, A. Malik, J. Agren, G. Amberg, and A. Borgenstam: *Acta Mater.*, 2012, vol. 60, pp. 1538–47.
30. A. Malik, H.K. Yeddu, G. Amberg, A. Borgenstam, and J. Agren: *Mater. Sci. Eng., A*, 2012, vol. 556, pp. 221–32.
31. H.K. Yeddu, A. Borgenstam, and J. Agren: *Acta Mater.*, 2013, vol. 61, pp. 2595–2606.
32. A. Malik, G. Amberg, A. Borgenstam, and J. Agren: *Acta Mater.*, 2013, vol. 61, pp. 7868–80.
33. M. Mamivand, M.A. Zaeem, H.E. Kadiri, and L.Q. Chen: *Acta Mater.*, 2013, vol. 61, pp. 5223–35.
34. M. Li, R.J. Zhang, and J. Allison: in *Magnesium Technology 2010*, Sean R. Agnew, Neale R. Neelameggham, Eric A. Nyberg, and Wim H. Sillekens, eds., TMS, Seattle, 2010, pp. 623–27.
35. J.S. Wang, M. Li, B. Ghaffari, L.Q. Chen, J.S. Miao, and J. Allison: *Mg2012: 9th Int. Conf. Magnes. Alloys Appl.*, W.J. Poole and K.U. Kainer, eds., Vancouver, Canada, 2012, pp. 163–70.
36. Y. Gao, H. Liu, R. Shi, N. Zhou, Z. Xu, Y.M. Zhu, J.F. Nie, and Y. Wang: *Acta Mater.*, 2012, vol. 60, pp. 4819–32.
37. H. Liu, Y. Gao, J.Z. Liu, Y.M. Zhu, Y. Wang, and J.F. Nie: *Acta Mater.*, 2013, vol. 61, pp. 453–66.
38. G.M. Han, Z.Q. Han, A.A. Luo, S.K. Sachdev, and B.C. Liu: *Acta Metall. Sin.*, 2013, vol. 49, pp. 277–83.
39. G.M. Han, Z.Q. Han, A.A. Luo, S.K. Sachdev, and B.C. Liu: *Scripta Mater.*, 2013, vol. 68, pp. 691–94.
40. S.G. Kim, W.T. Kim, and T. Suzuki: *Phys. Rev. E: Stat. Phys.*, 1999, vol. 60, pp. 7186–97.
41. P. Liang, H.L. Su, P. Donnadieu, M. Harmelin, and A. Quivy: *Z. Metall.*, 1998, vol. 89, pp. 536–40.
42. Y. Zhong, M. Yang, and Z.K. Liu: *CALPHAD*, 2005, vol. 29, pp. 303–11.
43. A.G. Khachaturyan: *Theory of Structural Transformations in Solids*, Wiley, New York, 1983, pp. 198–212.
44. B. Kouchmeshky and N. Zabaras: *Comput. Mater. Sci.*, 2009, vol. 45, pp. 1043–51.
45. G.B. McFadden, A.A. Wheeler, R.J. Braun, S.R. Coriell, and R.F. Sekerka: *Phys. Rev. E: Stat. Phys.*, 1993, vol. 60, pp. 2016–24.
46. A. Kazaryan, Y. Wang, S.A. Dregia, and B.R. Patton: *Phys. Rev. B: Condens. Matter.*, 2000, vol. 61, pp. 14275–78.
47. A. Kazaryan, Y. Wang, S.A. Dregia, and B.R. Patton: *Phys. Rev. B: Condens. Matter*, 2001, vol. 63, pp. 184102–11.
48. S.Y. Hu, J. Murray, H. Weiland, Z.K. Liu, and L.Q. Chen: *CALPHAD*, 2007, vol. 31, pp. 303–12.
49. S.Y. Hu: Ph.D. Thesis, Pennsylvania State University, 2004.
50. Y.Z. Ji, A. Issa, T.W. Heo, J.E. Saal, C. Wolverton, and L.Q. Chen: *Acta Mater.*, 2014, vol. 76, pp. 259–71.
51. R.E. Newnham: *Properties of Materials: Anisotropy, Symmetry, Structure*, Oxford University Press, Oxford, 2005, pp. 110–13.
52. S. Celotto: Ph.D. Thesis, University of Queensland, Australia, 1997.
53. L. Zhang, L.Q. Chen, and Q. Du: *Phys. Rev. Lett.*, 2007, vol. 98, p. 265703.
54. L. Zhang, L.Q. Chen, and Q. Du: *Acta Mater.*, 2008, vol. 56, pp. 3568–76.
55. C. Shen, J.P. Simmons, and Y. Wang: *Acta Mater.*, 2006, vol. 54, pp. 5617–30.
56. C. Shen, J.P. Simmons, and Y. Wang: *Acta Mater.*, 2007, vol. 55, pp. 1457–66.
57. M.X. Zhang and P.M. Kelly: *Scripta Mater.*, 2003, vol. 48, pp. 647–52.
58. J.F. Nie: *Scripta Mater.*, 2003, vol. 48, pp. 1009–15.
59. A. Biswas, D.J. Siegel, C. Wolverton, and D.N. Seidman: *Acta Mater.*, 2011, vol. 59, pp. 6187–204.
60. B.A. Chen, G. Liu, R.H. Wang, J.Y. Zhang, L. Jiang, J.J. Song, and J. Sun: *Acta Mater.*, 2013, vol. 61, pp. 1676–90.